applied optics

Modulation format identification of optical signals: an approach based on singular value decomposition of Stokes space projections

Rania A. Eltaieb,[1,*] Heba A. E. Abouelela,[7] Waddah S. Saif,[4,5] Amr Ragheb,[4]
Ahmed E. A. Farghal,[6] Hossam El-din H. Ahmed,[1] Saleh Alshebeili,[4,5]
Hossam M. H. Shalaby,[2,3] and Fathi E. Abd El-Samie[1,8]

[1]Department of Electronics and Electrical Communications Engineering, Faculty of Electronics Engineering, Menoufia University, Menouf 32952, Egypt
[2]Electrical Engineering Department, Alexandria University, Alexandria 21544, Egypt
[3]Department of Electronics and Communications Engineering, Egypt-Japan University of Science and Technology (E-JUST), Alexandria 21934, Egypt
[4]KACST-TIC in Radio Frequency and Photonics for the e-Society, King Saud University, Riyadh 11451, Saudi Arabia
[5]Department of Electrical Engineering, King Saud University, Riyadh 11421, Saudi Arabia
[6]Electrical Engineering Department, Faculty of Engineering, Sohag University, 82524 Sohag, Egypt
[7]Egyptian Ministry of Health and Population, Cairo, Egypt
[8]Department of Information Technology, College of Computer and Information Sciences, Princess NourahBint Abdulrahman University, Riyadh 21974, Saudi Arabia
*Corresponding author: rania-antar@el-eng.menofia.edu.eg

In this paper, two Stokes space (SS) analysis schemes for modulation format identification (MFI) are proposed. These schemes are based on singular value decomposition (SVD) and Radon transform (RT) for feature extraction. The singular values (SVs) are extracted from the SS projections for different modulation formats to discriminate between them. The SS projections are obtained at different optical signal-to-noise ratios (OSNRs) ranging from 11 to 30 dB for seven dual-polarized modulation formats. The first scheme depends on the SVDs of the SS projections on three planes, while the second scheme depends on the SVDs of the RTs of the SS projections. Different classifiers including support vector machine (SVM), decision tree (DT), and K-nearest neighbor (KNN) for MFI based on the obtained features are used. Both simulation and experimental setups are arranged and tested for proof of concept of the proposed schemes for the MFI task. Complexity reduction is studied for the SVD scheme by applying the decimation of the projections by two and four to achieve an acceptable classification rate, while reducing the computation time. Also, the effect of the variation of phase noise (PN) and state of polarization (SoP) on the accuracy of the MFI is considered at all OSNRs. The two proposed schemes are capable of identifying the polarization multiplexed modulation formats blindly with high accuracy levels up to 98%, even at low OSNR values of 12 dB, high PN levels up to 10 MHz, and SoP up to 45°. © 2020 Optical Society of America

https://doi.org/10.1364/AO.388890

1. INTRODUCTION

Changing the data rate of transmission in wireless communication systems is important, as fading and multiple paths are instrumental factors. However, in optical communications we receive different data rates because future networks will be heterogeneous. That is, each network has its own data rate, as the rate is required for proper demodulation or routing [1]. The upcoming optical communication systems are required to provide intelligent coherent receivers that are equipped with machine learning tools. Several researchers have applied machine learning to optical communication systems for determining the optical signal-to-noise ratio (OSNR), bit rate, modulation format, and other optical performance monitoring parameters [2–6].

The adaptivity represented in changing the modulation format and data rate of optical communication systems is required to cope with variations in channel states and user requirements [7]. There is a need to save the available bandwidth for data transmission only. Hence, a reduction of the amount of side information is very necessary. This can be guaranteed through blind modulation format identification (MFI)

schemes. Therefore, blindly identifying the modulation format at the receiver side allows the elimination of handshaking information between the transmitter and the receiver. Additionally, the optical fiber effects such as phase noise (PN), state of polarization (SoP), and OSNRs are challenging effects for the MFI task. Intelligent receivers for addressing the MFI task with different challenging issues are addressed in [8].

The MFI task can be determined with and without side information. In the information-aided scenario, side information such as pilot tone and frequency offset difference have been used [9,10]. On the other hand, in the absence of side information, the MFI is blind.

The literature on blind MFI can be divided into two main categories based on the space of representation of optical signals. Both Jones space and Stokes space (SS) have been used for blind MFI. The first trend depends on the processing of optical signals directly or the images extracted from the signals such as eye diagrams and constellation diagrams [11–14]. The second trend depends on either the optical signals or the projections of these signals on definite planes of the Poincare sphere [15–18].

Adles *et al.* [11] provided an approach for MFI based on the histogram of the electric field distribution. This approach achieved high recognition rates, but its computation process is complex. Bilal *et al.* [12] used the peak-to-average power ratio

determined from the samples of the received data for modulation format classification. The OSNR information is required prior to the classification process. Liu *et al.* [13] introduced a nonlinear power transformation and peak detection algorithm to perform MFI. The Fourier transform is calculated for the modulated data. This method has provided high accuracy of identification, but it requires a large number of samples in the identification process. Eltaieb *et. al.* [14] provided a study of the MFI based on Jones space representation, singular value decomposition (SVD), and radon transform (RT). The SVD and RT are used with the constellation diagrams of different single- and dual-polarized (DP) modulation formats. This method provides a high level of accuracy for MFI even with high PN and SoP levels. The SS has captured the interest of several researchers as in [15–18] due to its immunity to the carrier PN and the polarization mixing [17]. All these methods that utilized the SS for MFI achieved high accuracy levels, but with high complexity due to the multiple classification steps.

In this paper, due to the importance of choosing the right modulation format for data transmission in optical communication systems, blind MFI is studied. The MFI is performed in the SS based on both SVD and RT concepts. Utilization of the SS is attributed to its main advantages of immunity to PN and signal rotations [19,20]. The projections of data on three planes
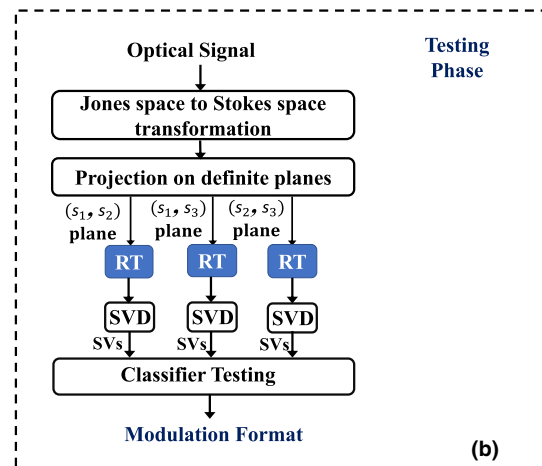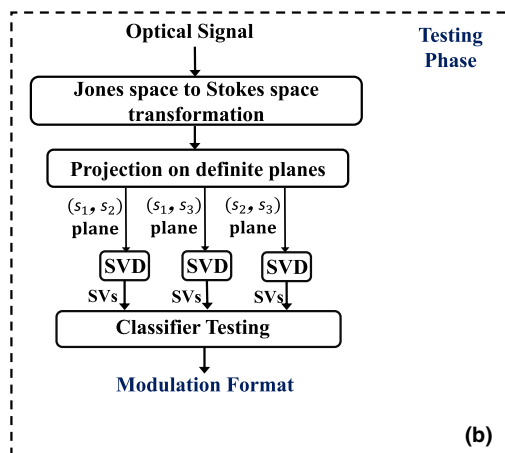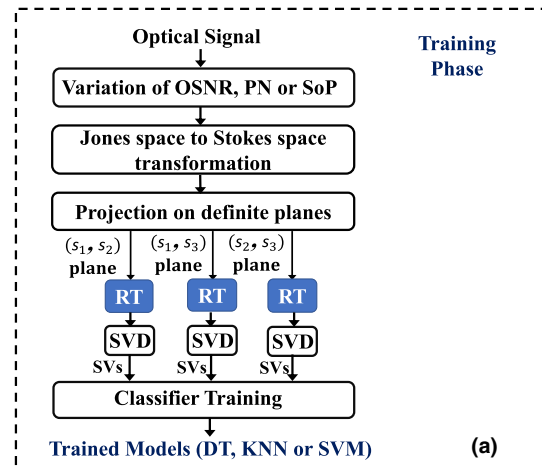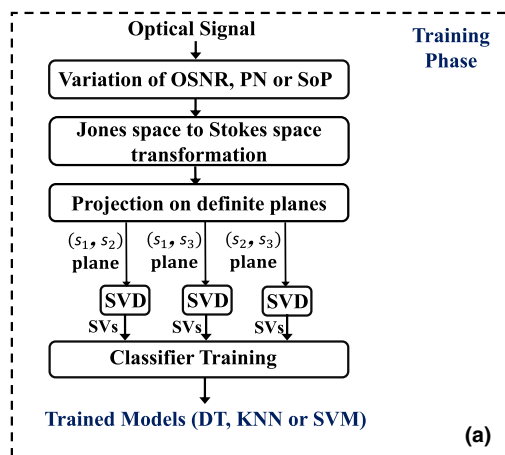

Fig. 1. Block diagram of the proposed MFI scheme based on SVDs of SS planes.

Fig. 2. Block diagram of the proposed MFI scheme based on SVDs of RTs of SS planes.
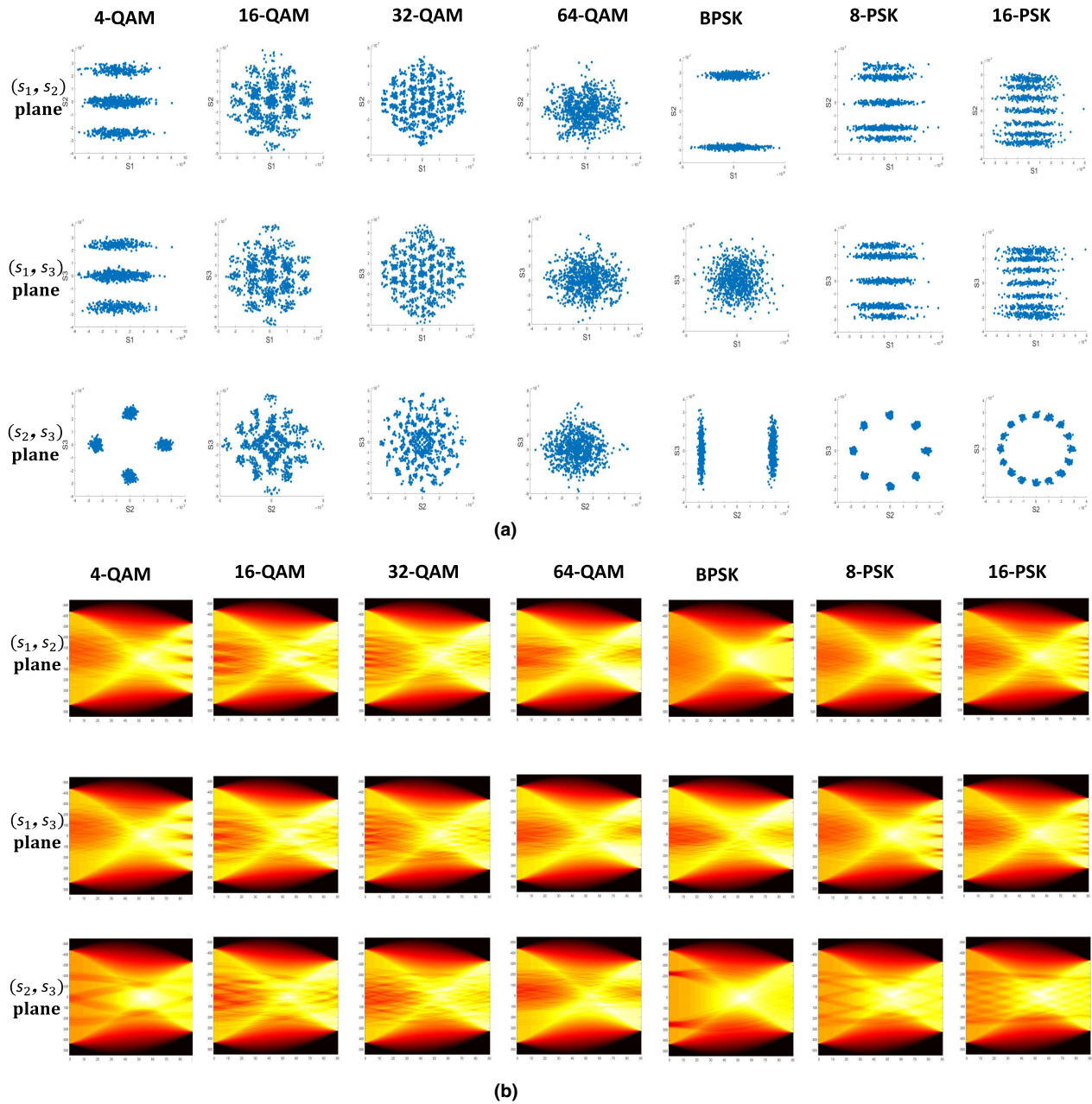
(a)

(b)

Fig. 3. Examples of the used images for seven modulation formats. The OSNR is 30 dB, and the number of samples is 1024. (a) SS images on the three used planes, (s_1, s_2), (s_1, s_3), and (s_2, s_3). (b) RTs of all images shown in (a).

in SS representation are obtained, namely, (s_1, s_2) plane, (s_1, s_3) plane, and (s_2, s_3) plane. These projections are dealt with as images. The singular values (SVs) of these images are extracted and used for MFI. Different classifiers are trained and tested for the MFI task. Furthermore, complexity reduction through decimation is performed on the images of the three planes prior to MFI to reduce complexity. The rest of this paper is organized as follows. The SS analysis is presented in Section 2. Section 3 is devoted to the proposed SVD-based MFI from the three used planes and the mathematical representation of the RT for optical MFI. In Section 4, a complexity reduction approach for the classification process based on the decimation of projected images

prior to estimation of the SVs is presented. In Section 5, both simulation and experimental setups are presented. Section 6 provides the numerical results, including simulation results with 1024 and 2048 samples (Section 6.A) and simulation and experimental results with 1024 samples (Section 6.B). Finally, the conclusion is given in Section 7.

2. STOKES SPACE ANALYSIS

The Jones vectors of the optical signal are complex, and they can be transformed to another representative space, i.e., SS. The SS representation gives four parameters that lead to the recovery
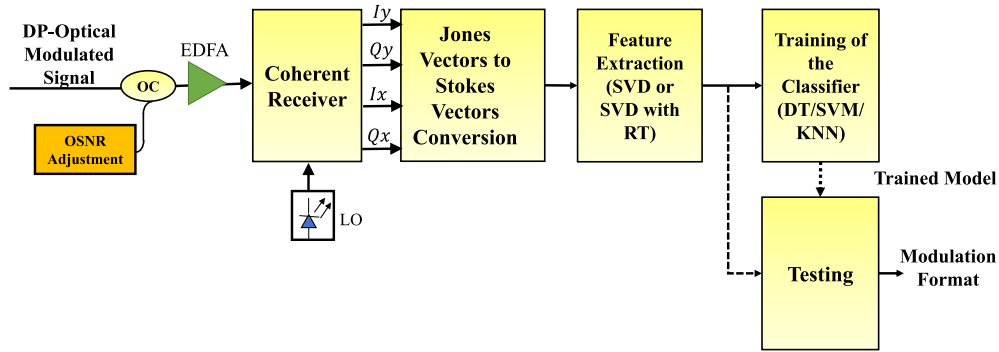
Fig. 4. Simulation system setup for the proposed MFI schemes. DP, dual-polarized; EDFA, erbium-doped fiber amplifier; LO, local oscillator; MZM, Mach–Zehnder modulator; OC, optical coupler; SSMF, standard single-mode fiber; SVD, singular value decomposition; RT, radon transform; DT, decision tree; KNN, K-nearest neighbor; SVM, support vector machine.
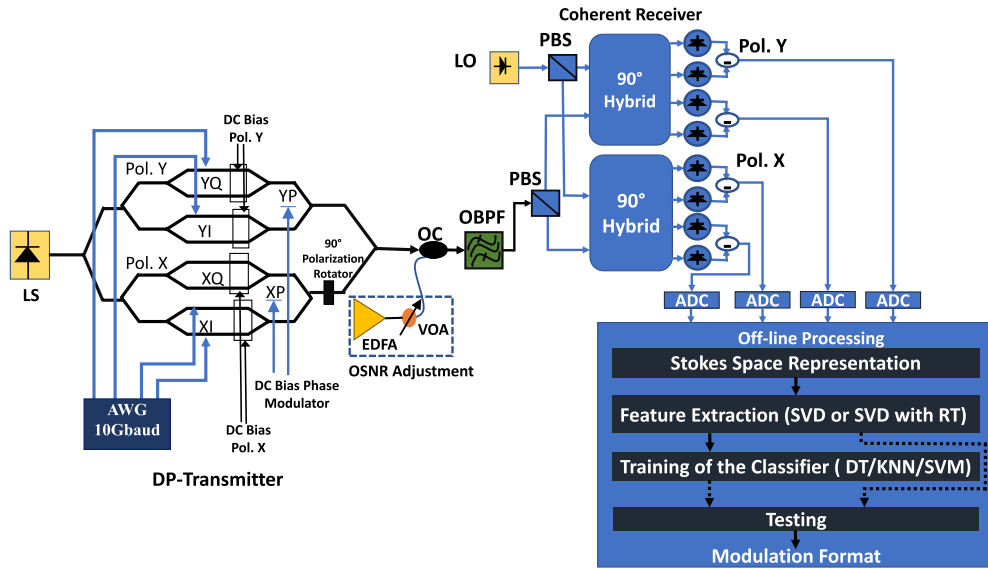

Fig. 5. Experimental setup of the demonstrated optical MFI using the proposed schemes. LS, laser source; AWG, arbitrary waveform generator; XI, XQ, YI, and YQ, Mach–Zehnder sub-modulators of x and y polarizations; XP and YP, phase modulators; EDFA, erbium-doped fiber amplifier; VOA, variable optical attenuator; OC, optical coupler; OBPF, optical band-pass filter; LO, local oscillator; PBS, polarization beam splitter; ADC, analog-to-digital converter.

of the existing SoP in the optical signal. These four parameters are s_o, s_1, s_2, and s_3. The s_o represents the total power of the incoming optical signal, while s_1, s_2, and s_3 represent the 0° linear, 45° linear, and circularly polarized light, respectively. The combination of s_1, s_2, and s_3 gives the Poincare sphere representation. The Jones vectors to Stokes vectors, S, conversion is performed as follows [19]:

$$S = \frac{1}{2} \begin{bmatrix} s_o \\ s_1 \\ s_2 \\ s_3 \end{bmatrix} = \frac{1}{2} \begin{bmatrix} e_x e_x^* + e_y e_y^* \\ e_x e_x^* - e_y e_y^* \\ e_x^* e_y + e_x e_y^* \\ -j e_x^* e_y + j e_x e_y^* \end{bmatrix} = \frac{1}{2} \begin{bmatrix} a_x^2 + a_y^2 \\ a_x^2 - a_y^2 \\ 2 a_x a_y \cos \Delta\phi \\ 2 a_x a_y \sin \Delta\phi \end{bmatrix},$$

(1)

where e_x and e_y are the horizontal and vertical optical waves, respectively. a_x and a_y are the amplitudes, and ϕ_x and ϕ_y are the phases of the Jones vector components, e_x and e_y, respectively. $\Delta\phi = \phi_x - \phi_y$ is the phase difference between e_x and e_y.

3. PROPOSED MFI SCHEMES

Figure 1 shows the block diagram of the proposed SVD-based scheme for optical MFI from SS. As shown in Fig. 1(a), there is a need for both training and testing phases. The number of the used samples is determined first. It is taken as 1024 and 2048 samples in this study. The channel impairments—OSNR, PN, and SoP—are considered in the processing. Then, the incoming signal is converted from the Jones space to the SS by implementing the projection on three planes, namely, (s_1, s_2), (s_1, s_3), and (s_2, s_3). These projections are treated as images and used for feature extraction. The SVs are extracted from these images with the SVD algorithm. These SVs are used to train the used machine learning classifiers, namely, a support vector machine (SVM), K-nearest neighbor (KNN), and decision tree (DT) [8]. The same steps are followed for the testing phase to measure the model accuracy of identification, as shown in Fig. 1(b).
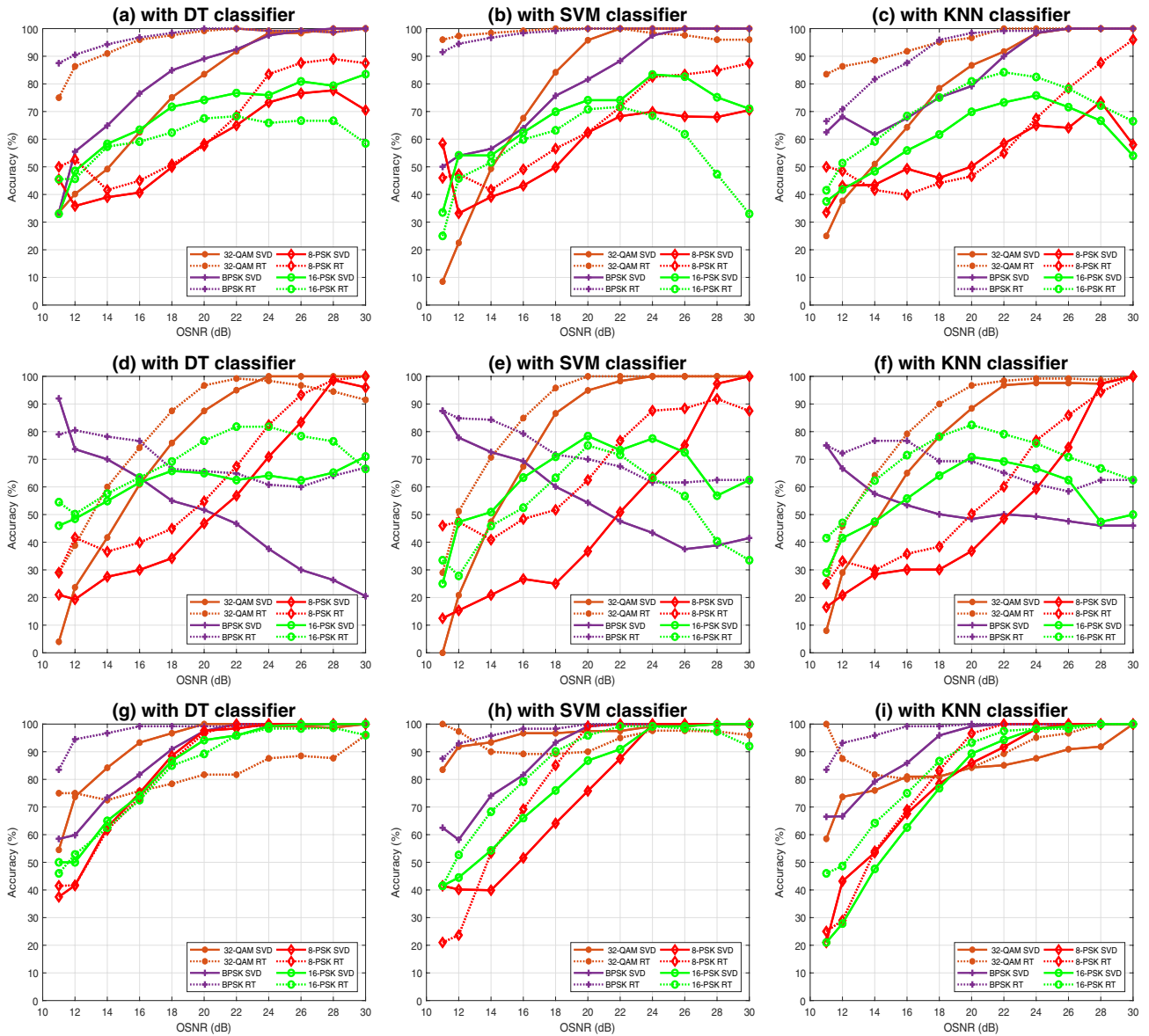
Fig. 6. Accuracy versus OSNR for four modulation formats with 1024 samples for SVD and SVD with RT schemes in the absence of PN with: (a)–(c) (s_1, s_2) plane; (d)–(f) (s_1, s_3) plane; and (g)–(i) (s_2, s_3) plane.

Specifically, each projection is captured as a color image and stored in a bmp format. A gray-scale image is obtained from this color image to reduce the computational load. The SVD of the gray-scale image produces three matrices, namely, **U**, **S**, and **V**, as follows [21]:

$$\mathbf{I} = \mathbf{U}\mathbf{S}\mathbf{V}^T, \tag{2}$$

where **U** and **V** are the left and right singular vectors of the matrix **I** representing the projected image matrix, respectively, and T denotes the transpose. The diagonal elements of the matrix **S** constitute the feature vector.

Other types of images can be generated from these projection planes to obtain more discriminative features by evaluating the RTs of the projected images. The main steps followed to get the RTs are shown in Fig. 2. The training and testing phases are applied for the MFI task using the RTs. In the training phase

in Fig. 2(a), a similar manner is followed as in Fig. 1 to get the projected images. The RTs of these images are constructed and used as images also, and they can be calculated using Eq. (3). The SVD is applied to these new RTs, and their SVs are extracted as the dominant features. These features are used for the training of the classifiers. The testing phase is shown in Fig. 2(b). It has the same sequence as in the training except that after determination of the SVs, the test of the trained classifiers is performed. The sequence of training and testing is performed on the three planes, and the best plane for MFI is selected. The RT is calculated by [22,23]

$$R(t, \theta) = \int_{-\infty}^{\infty} \int_{-\infty}^{\infty} I(x, y)\delta\left[t - x\cos(\theta) - y\sin(\theta)\right] dx dy, \tag{3}$$

where $I(x, y)$ is the projected image, x and y represent the coordinate positions, $R(t, \theta)$ is the RT image, t is the normal from the origin to the line of projection, θ is the projection angle, which is the angle between the normal and the horizontal axis of the image, and $\delta(\cdot)$ is the Dirac delta function. The RT is evaluated by the summation of all values in the matrix, taking into consideration the angle of projection. In this paper, the projection angle is taken from 0° to 90° due to the similarity property of the RT.

Examples of the projected images on the three planes and their RTs are shown in Fig. 3 for seven types of modulation formats with 1024 samples: 4-quadrature amplitude modulation (4-QAM), 16-QAM, 32-QAM, 64-QAM, binary phase-shift keying (BPSK), 8-PSK, and 16-PSK at 30 dB. It is clear that each modulation format has its own signature even in the projected image or in its RT. In the RT, each point is transformed to a curved line, and the number of lines produced gives the same number of existing groups of points in the planes of projection. The higher-order modulation formats are hard to identify in the SS due to their large numbers of point groups.
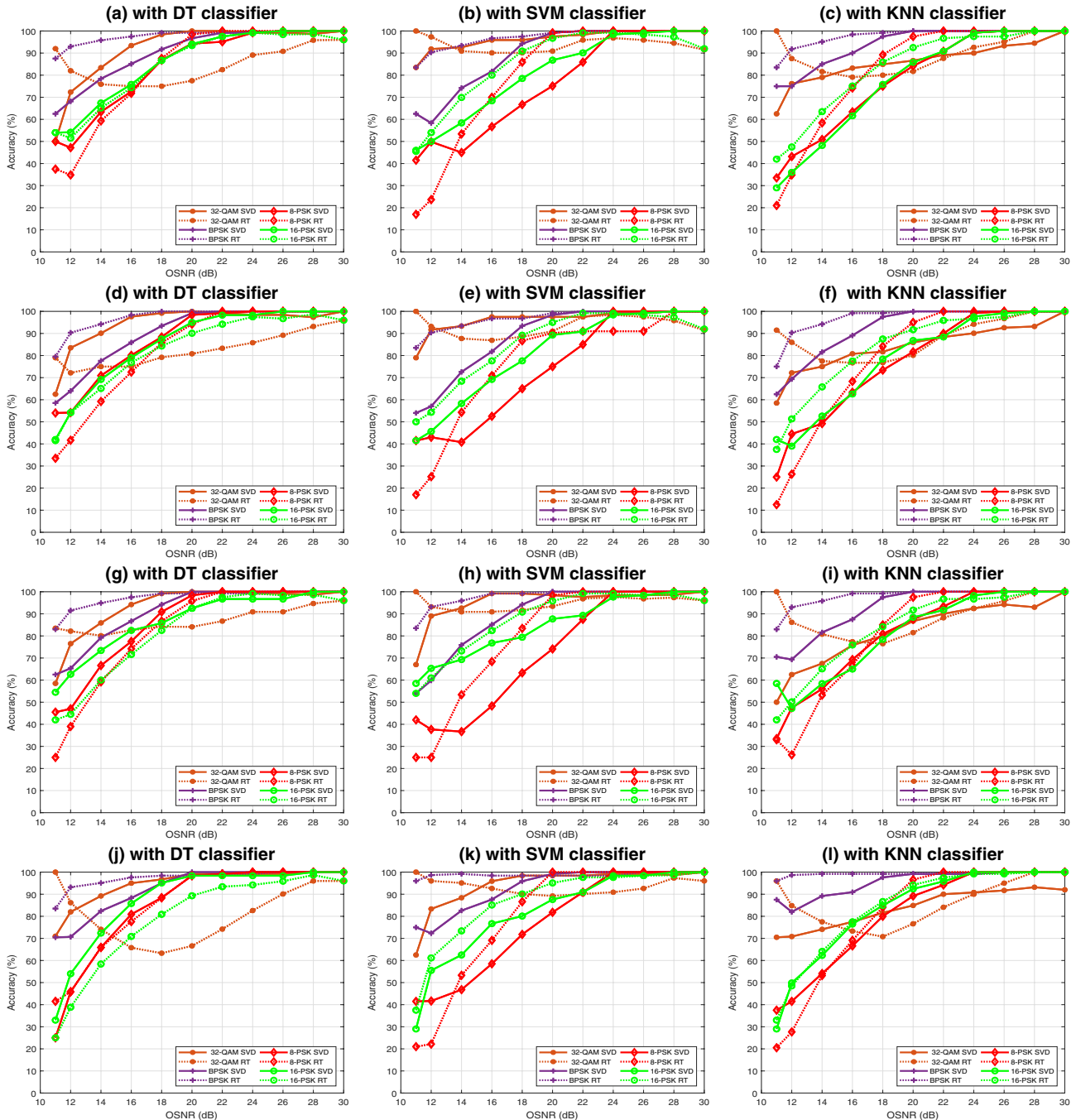

Fig. 7. Accuracy versus OSNR for four modulation formats with 1024 samples for SVD and SVD with RT schemes with (s_2, s_3) plane at PNs of: (a)–(c) 1 kHz; (d)–(f) 10 kHz; (g)–(i) 100 kHz; and (j)–(l) 1 MHz.
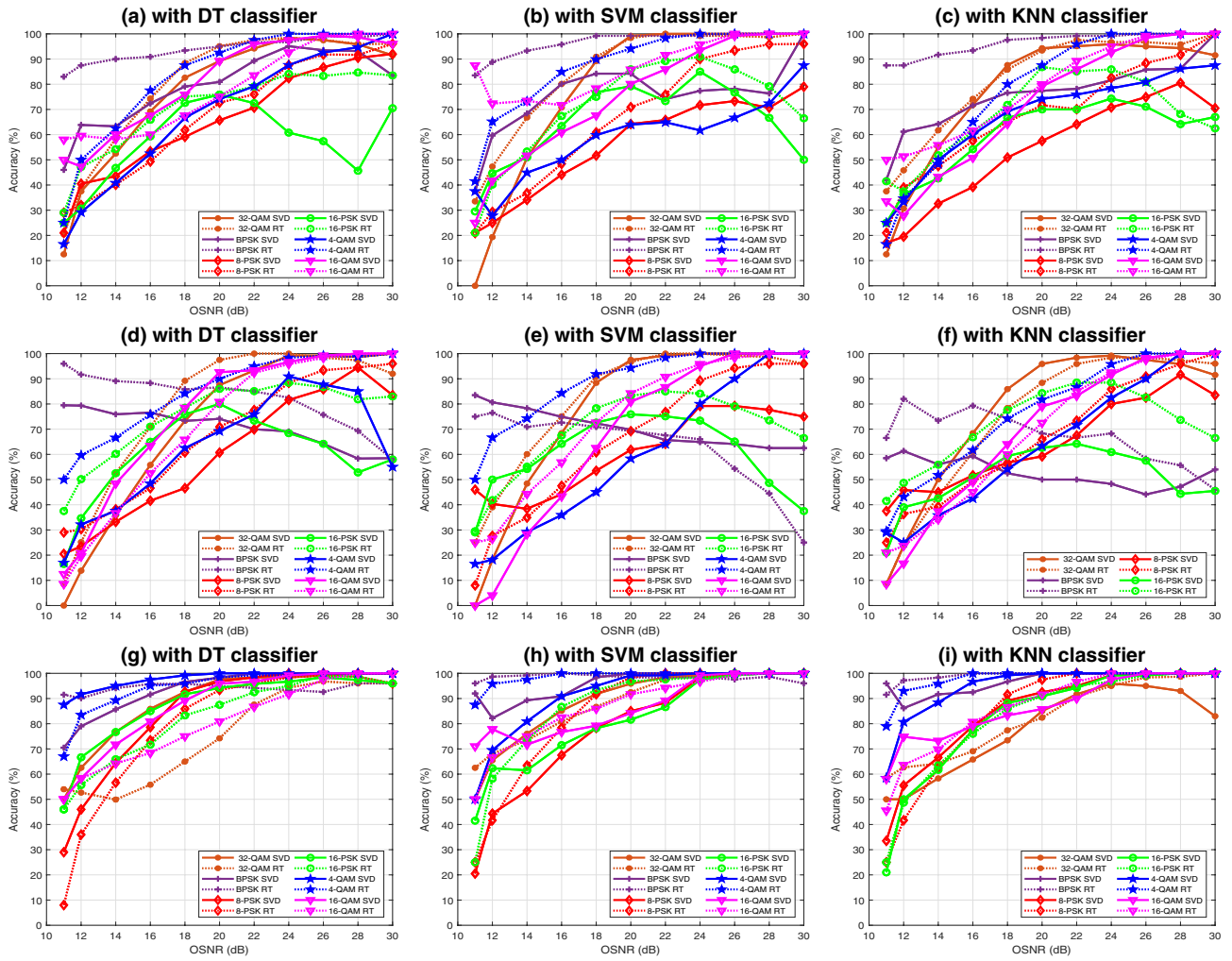
Fig. 8. Accuracy versus OSNR for six modulation formats with 2048 samples for SVD and SVD with RT schemes with the three planes in the absence of PNs of: (a)–(c) (s_1, s_2); (d)–(f) (s_1, s_3); and (g)–(i) (s_2, s_3) planes.

4. DECIMATION FOR COMPLEXITY REDUCTION

The complexity of the SVD is dependent on the computation cost, which is high owing to the number of computed SVs. The complexity reduction can be performed in different ways, one of them is reducing the sizes of the used images to reduce the number of required SVs in the computation process.

The sizes of the images are reduced by decimation of each one. The new decimated images are used with the proposed SVD scheme to extract their SV features and train the different classifiers for the MFI task. If the lexicographic ordering of a projected image is performed to yield a 1D vector **f**, the decimated images can be estimated as follows:

$$\mathbf{g} = \mathbf{D}\mathbf{f}, \tag{4}$$

where **D** is the decimation operator defined as $\mathbf{D} = \mathbf{D}_1 \circledast \mathbf{D}_1$. Here, $\circledast$ is the Kronecker product, and $\mathbf{D}_1$ is a 1D filtering and down-sampling operator for decimation by two [24]:

$$\mathbf{D}_1 = \frac{1}{2} \begin{bmatrix} 1 & 1 & 0 & 0 & \cdots & 0 & 0 \\ 0 & 0 & 1 & 1 & \cdots & 0 & 0 \\ \vdots & \vdots & \vdots & \vdots & \ddots & \vdots & \vdots \\ 0 & 0 & 0 & 0 & \cdots & 1 & 1 \end{bmatrix}. \tag{5}$$

If the original images in any of the three projection planes are of size $m \times n$, then the size of the new produced images from decimation by two and four will be $m/2 \times n/2$ and $m/4 \times n/4$, respectively. As seen in [25], the complexity of the SVD is considered to be of $O(m^2 n + n^3)$. Here, the complexity will be reduced after decimation by two and four to be of $O((\frac{m}{2})^2(\frac{n}{2}) + (\frac{n}{2})^3)$ and $O((\frac{m}{4})^2(\frac{n}{4}) + (\frac{n}{4})^3)$, respectively.

5. SIMULATION AND EXPERIMENTAL SETUPS

Figures 4 and 5 show the simulation and experimental setups for the SS schemes, respectively. The simulation setup is used to generate eight DP modulation formats, namely, 4-QAM, 16-QAM, 32-QAM, 64-QAM, BPSK, QPSK, 8-PSK, and 16-PSK, at 10 GBaud. For each modulation format, 1024 and 2048 samples are taken, and 40 images are collected at each OSNR value for each plane of projection. The OSNR is taken to be in the range of 11 dB to 30 dB with a 2 dB step. The transmission losses are compensated with an erbium-doped fiber amplifier (EDFA). At the receiver side, the signal is passed through an optical filter. A coherent detector, with balanced photo-detection (BPD), is used with a local oscillator (LO).
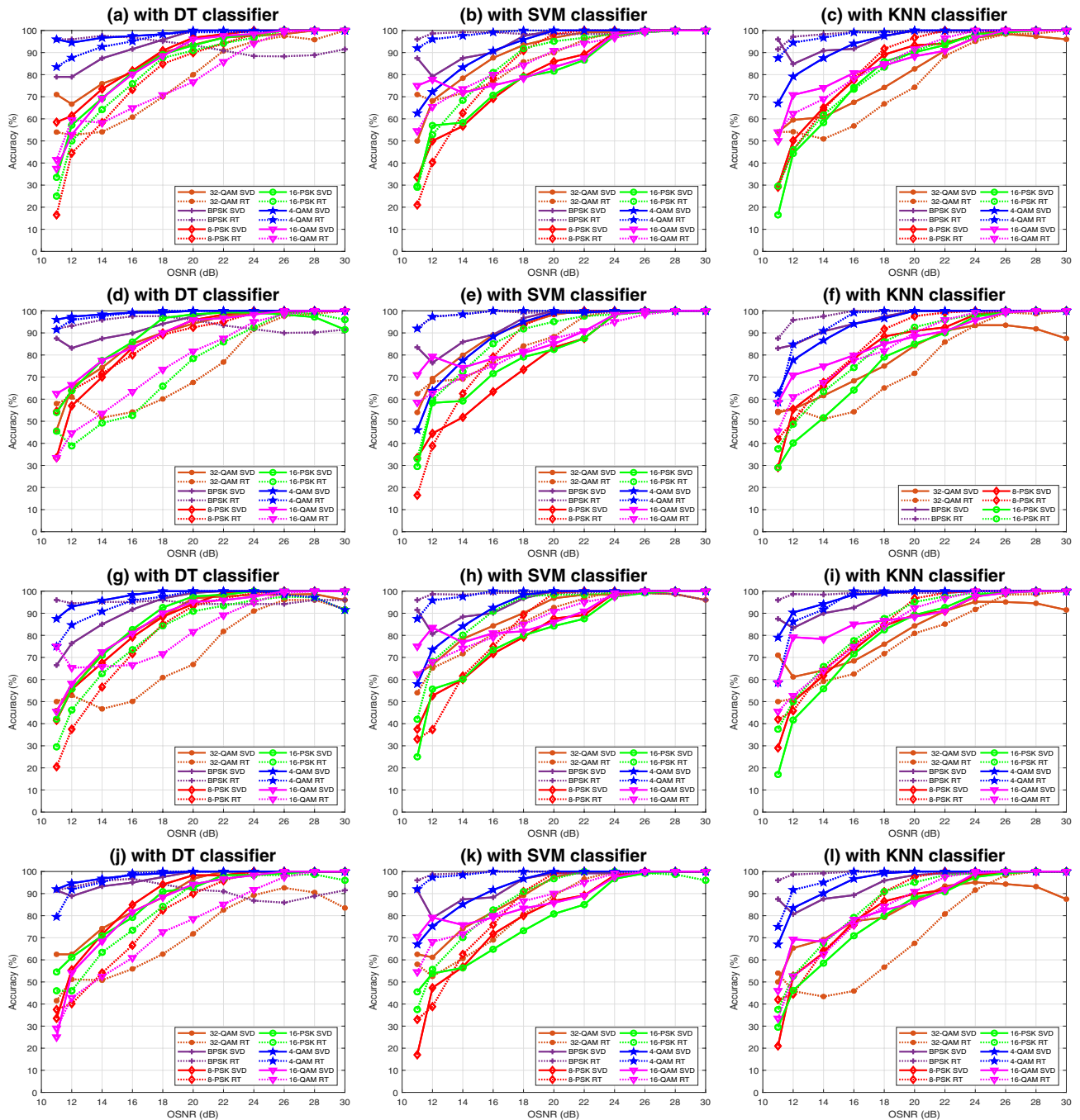
Fig. 9. Accuracy versus OSNR for six modulation formats with 2048 samples for SVD and SVD with RT schemes with (s_2, s_3) plane at PNs of: (a)–(c) 1 kHz; (d)–(f) 10 kHz; (g)–(i) 100 kHz; and (j)–(l) 1 MHz.

The collected signals are converted form the Jones vectors to the SS representation. The three planes of projection are utilized. The decimation of these images is considered, and also their RTs are evaluated. Finally, the classifiers are trained and tested with the features extracted from all types of produced images to measure the accuracy of the identification process.

To ensure the feasibility of the two proposed (SVD and SVD with RT) schemes for MFI in optical transmission systems, a proof-of-concept experiment is conducted using the setup shown in Fig. 5. A continuous-wave laser source

(NKTPhotonics) of 1550 nm and 15 dBm output power is used to drive a DP IQ (Fujitsu FTM7977HQA) Mach–Zehnder modulator (MZM). A Keysight M9185A arbitrary waveform generator (AWG) is used to provide pseudo-random binary sequences (PRBS) of a word pattern $(2^{11}-1)$ to generate four multi-level electrical signals of 64 GSa/s. The transmitted optical modulation formats include DP-4-QAM, DP-16-QAM, and DP-64-QAM.

To vary the OSNR of a received optical signal, the amplified spontaneous emission (ASE) output of an EDFA (Amonics
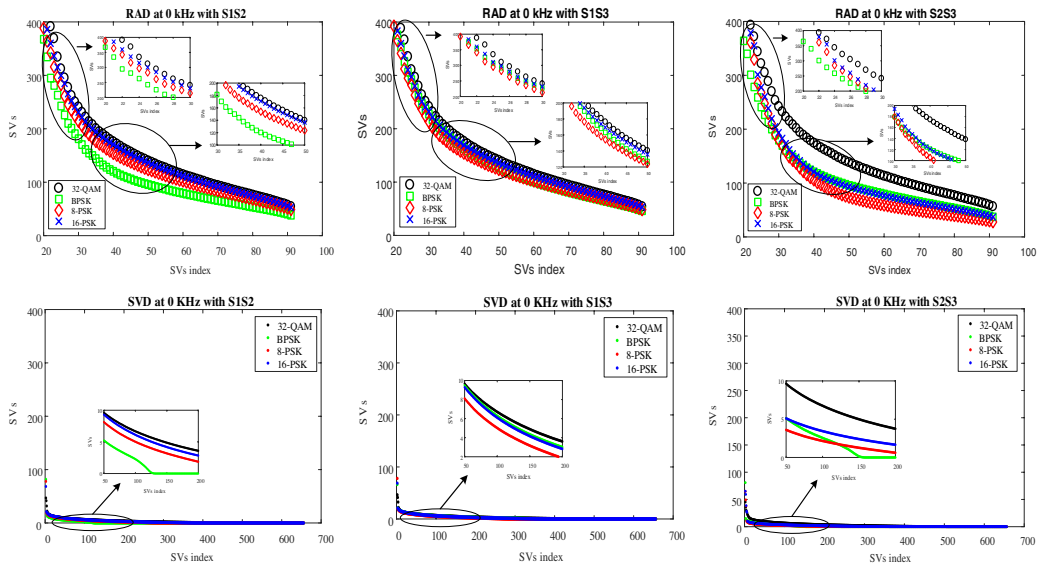
Fig. 10. Average SVs versus SV index for four modulation formats with 1024 samples at 30 dB. The first row is for the SVDs of RTS of the images, and the second row is for the SVD of the SS images in the three planes: (s_1, s_2); (s_1, s_3); and (s_2, s_3).
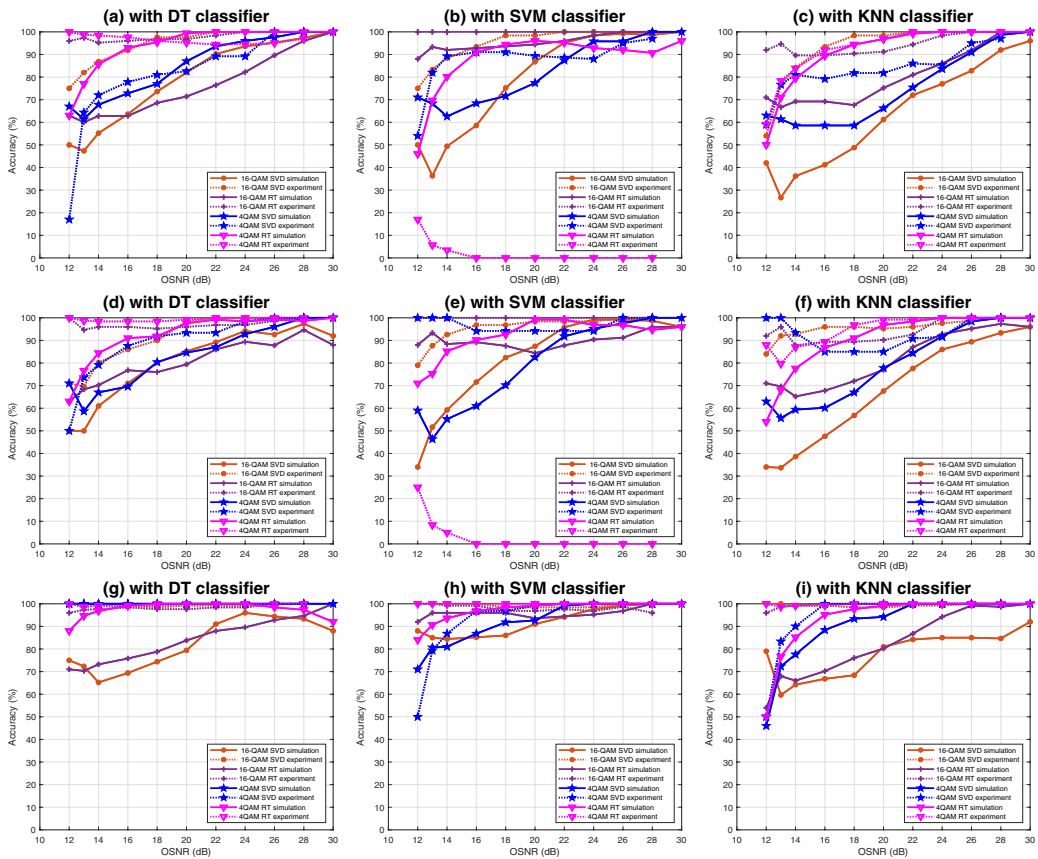

Fig. 11. Accuracy versus OSNR for two modulation formats for SVD and SVD with RT schemes with the three planes in the absence of PN effect of: (a)–(c) (s_1, s_2) plane; (d)–(f) (s_1, s_3) plane; and (g)–(i) (s_2, s_3) plane.

AEDFA-C-18B-R) is added to the optical signal using a 50:50 optical coupler. An optical attenuator (AO) is used to adjust the OSNR value. At the receiver side, a coherent receiver is employed and a Keysight digital storage oscilloscope

(DSOX93294A) is used as a signal digitizer. The stored received samples are processed offline, where SS representation, feature extraction, machine learning algorithms, and modulation identification are performed sequentially. The modulation formats
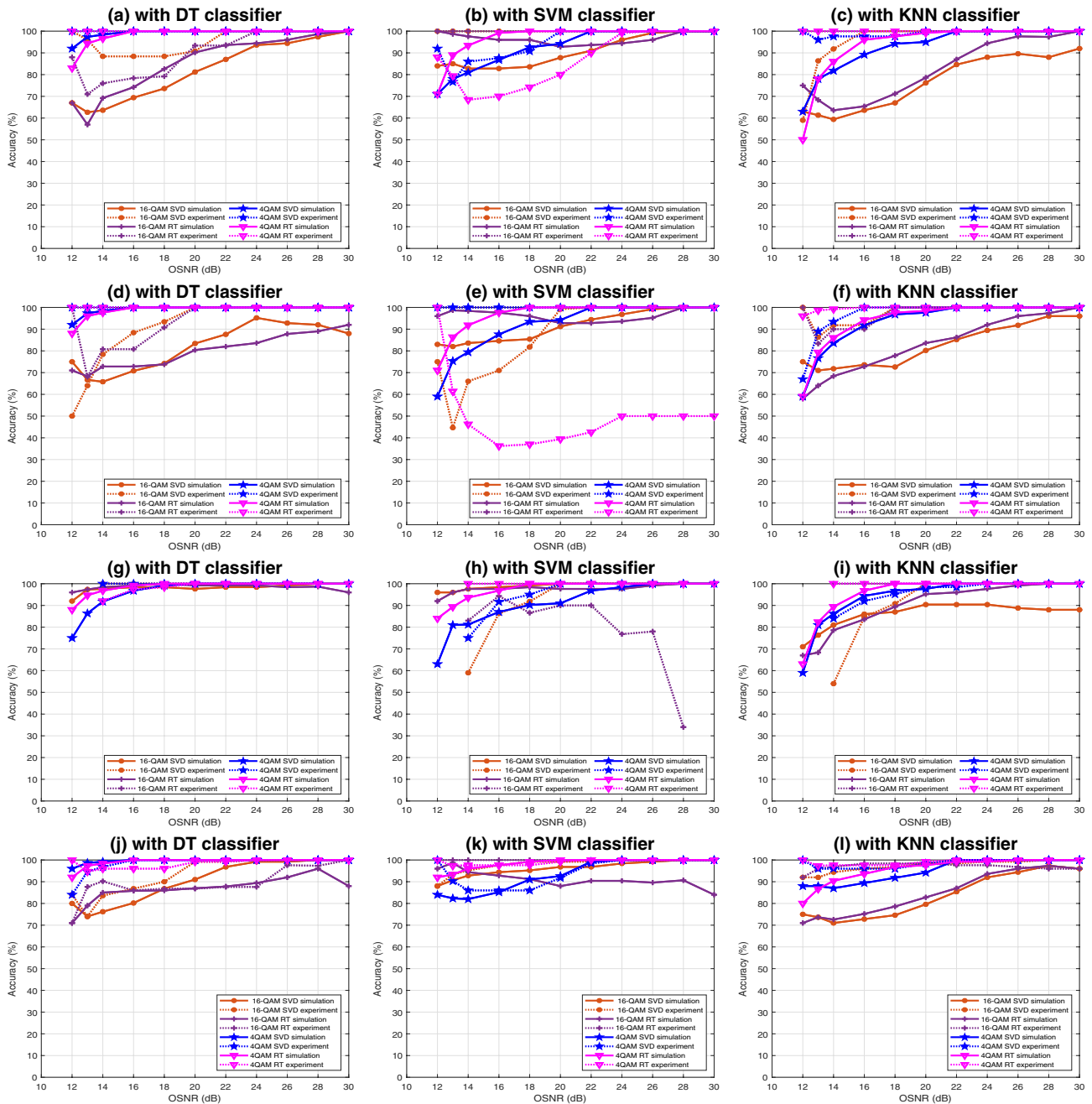
Fig. 12. Accuracy versus OSNR for two modulation formats for SVD and SVD with RT schemes with the (s_2, s_3) plane at PNs of: (a)–(c) 1 kHz; (d)–(f) 10 kHz; (g)–(i) 100 kHz; and (j)–(l) 1 MHz.

are identified using the KNN, DT, or SVM classifiers. The same images are collected, and their features (SVs) are used for training and testing of the classifiers. It is worth noting that the effect of channel impairments is taken into consideration, where the PN and SoP are utilized for MFI to determine the limits for the required accuracy levels.

6. RESULTS WITH 1024 AND 2048 SAMPLES

In Figs. 6–16, we present the results of MFI based on SS representation. The three planes are considered for the MFI based

on the SVs as the dominant features from the projected images and their RTs as shown in Figs. 6–12. The effect of decimation on these images is presented in Figs. 13 and 14. The variations in accuracy with the PN and SoP for six modulation formats are shown in Figs. 15 and 16, respectively.

A. Simulation Results with 1024 and 2048 Samples

Figure 6 reveals the accuracy versus the OSNR on the obtained optical signals with 1024 samples for four modulation formats, neglecting the effects of PN and SoP. For the three planes, the DT and KNN classifiers provide higher accuracy levels than
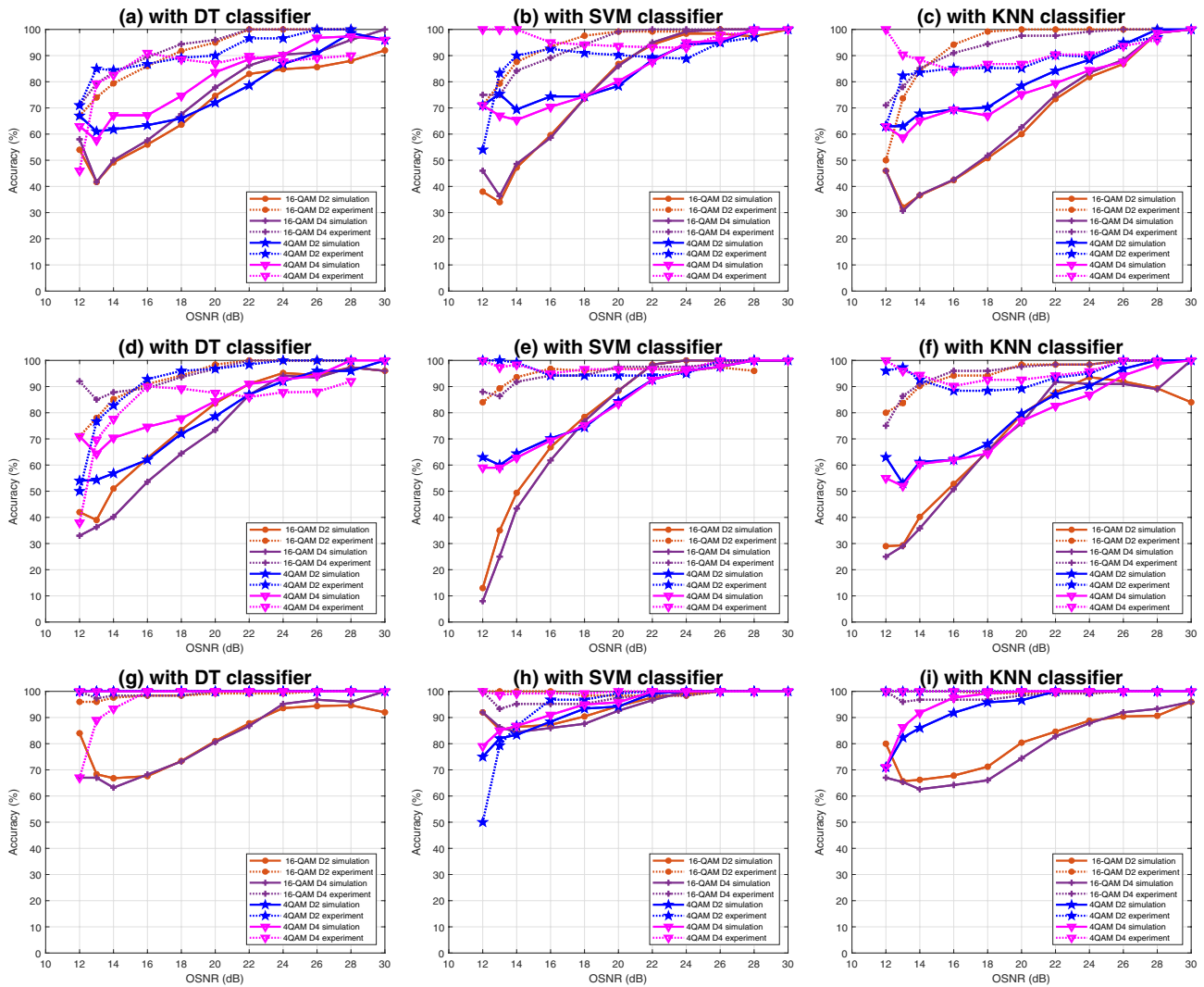
Fig. 13. Accuracy versus OSNR for two modulation formats with decimation by two and four for SVD scheme applied on the three planes in the absence of PNs of: (a)–(c) (s_1, s_2); (d)–(f) (s_1, s_3); and (g)–(i) (s_2, s_3).

those of the SVM classifier. High-order modulation formats require very high OSNRs to be identified, as a large number of ordered points is required. The RTs provide higher accuracy levels than those achieved with the projected images themselves, especially with the DT and KNN classifiers.

For the (s_1, s_2) plane with the DT classifier, 20 dB are required to get a 100% accuracy for the RTs of the BPSK and 32-QAM modulation formats. With the KNN classifier, 20 dB are required for BPSK and 32-QAM to reach a 98% accuracy level with both schemes. With the SVM classifier, BPSK and 32-QAM require 16 dB to reach a 98% accuracy level. The 8-PSK and 16-PSK modulation formats need OSNR levels larger than 30 dB to get a 90% accuracy level with all classifiers.

For the (s_1, s_3) plane, the three classifiers provide unacceptable accuracy levels with some modulation formats. For the (s_2, s_3) plane, the three classifiers provide high accuracy with the four modulation formats. For the DT and KNN classifiers, 20 dB and 22 dB are required for all modulation formats to reach a 90% accuracy level with the SVD and SVD with RT schemes,

respectively. For 32-QAM, 24 dB and 26 dB are required to get an accuracy level above 90% with the DT and KNN classifiers, respectively. For the SVM classifier, all modulation formats need 24 dB to reach a 98% accuracy level.

Figure 7 shows the accuracy versus OSNR for the (s_2, s_3) plane taking the PN effect into consideration. It is apparent that there are no significant changes in the accuracy of identification at the same OSNR for all PN values, because the PN effect on the images or their RTs does not produce large differences between them. The DT and KNN classifiers provide higher accuracies of identification than those obtained with the SVM classifier.

Figure 8 gives the accuracy versus OSNR from the three planes for six modulation formats with 2048 samples. The (s_2, s_3) plane provides the best accuracy levels with the three classifiers. Moreover, the DT and KNN classifiers provide better and more stable accuracy levels than those obtained with the SVM classifiers.
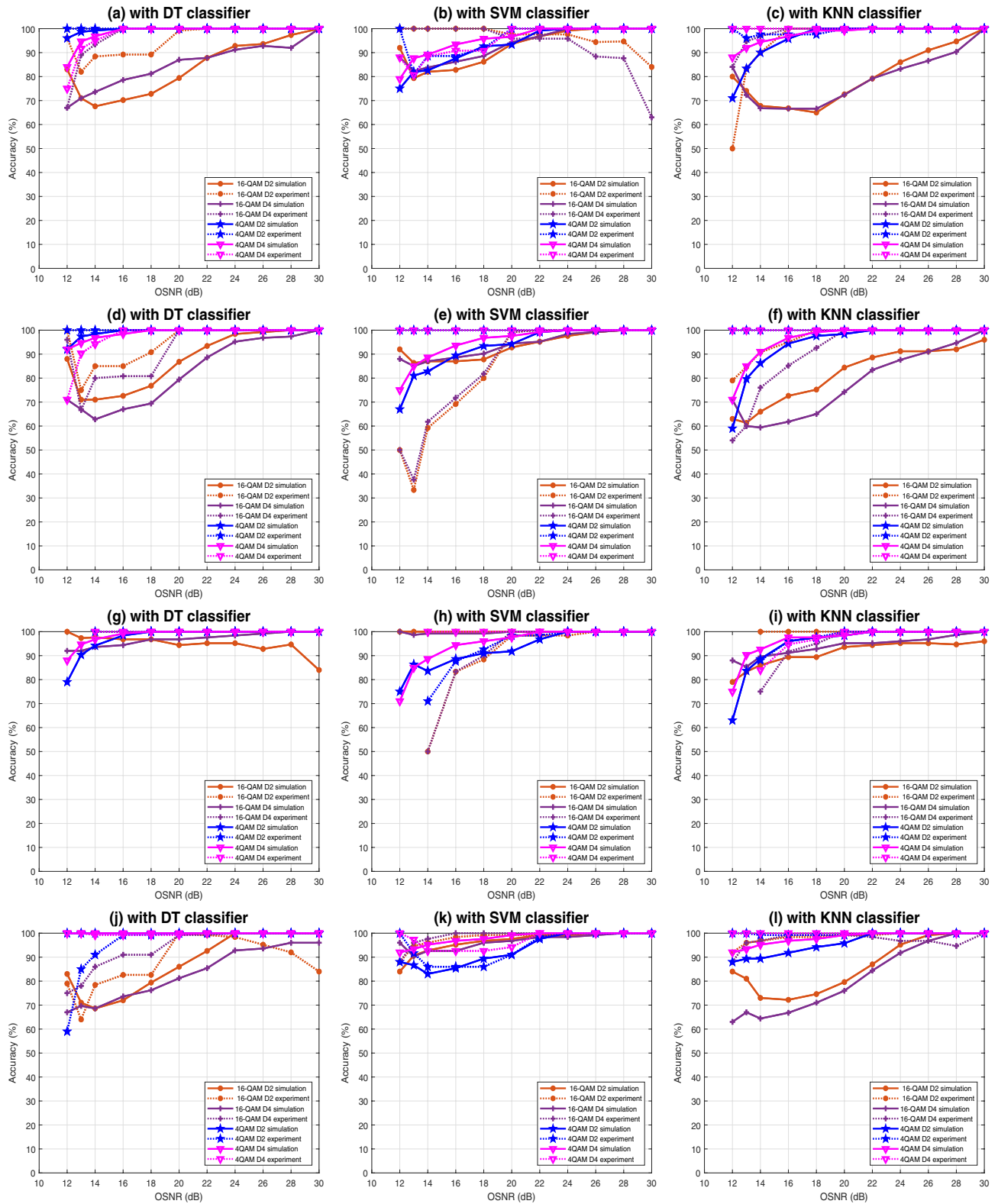
Fig. 14. Accuracy versus OSNR for two modulation formats with decimation by two and by four using SVD scheme with (s_2, s_3) plane at PNs of: (a)–(c) 1 kHz; (d)–(f) 10 kHz; (g)–(i) 100 kHz; and (j)–(l) 1 MHz.

Figure 9 shows the accuracy versus OSNR from the (s_2, s_3) plane taking the PN effect into consideration with 2048 samples. The three classifiers provide high and stable accuracy levels with all used modulation formats.

Figure 10 shows the average SV amplitude versus the SV index for better understanding of the results shown in Figs. 6–9. It is clear that the SVs are different for the four represented
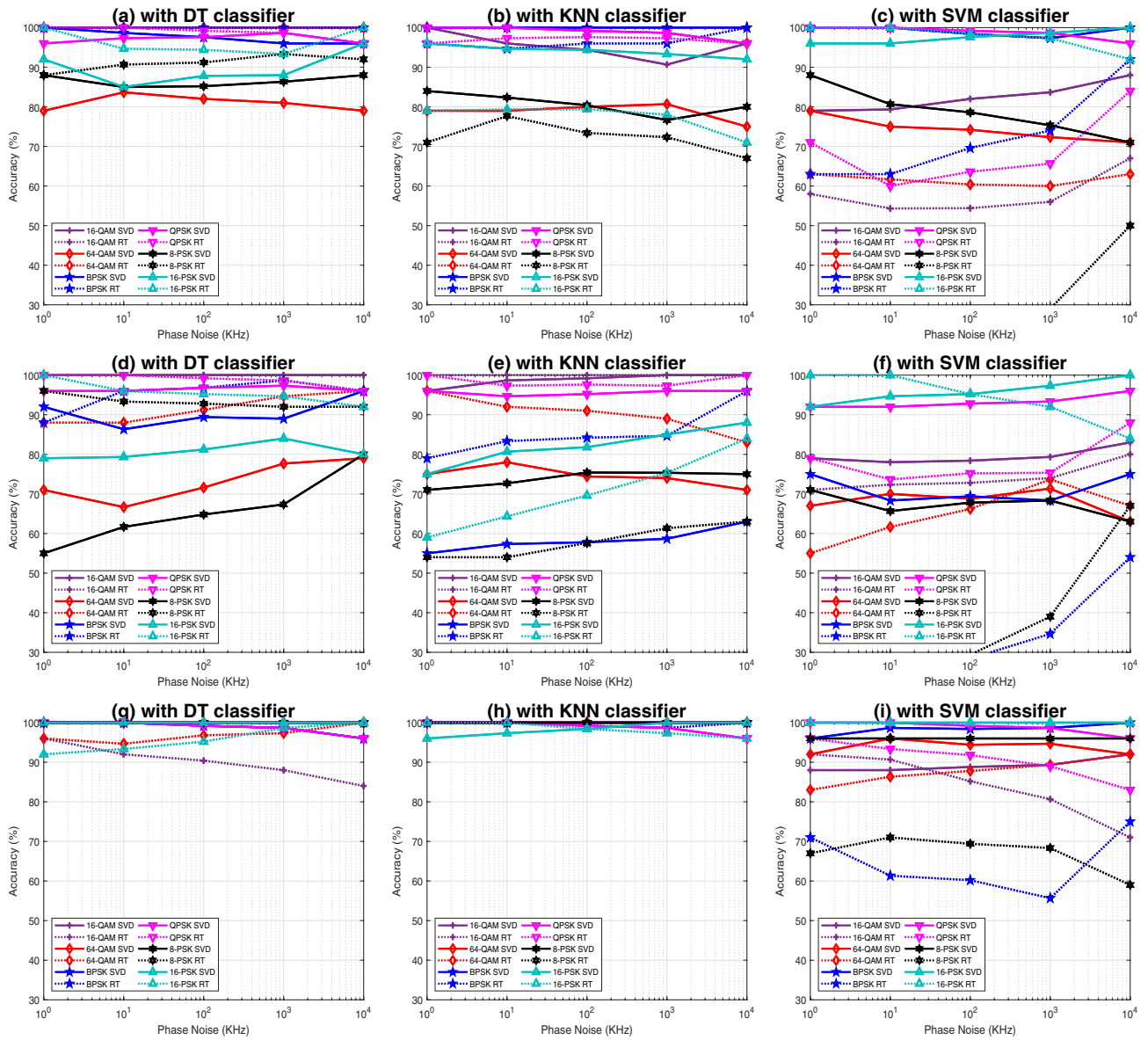
Fig. 15. Accuracy versus PN levels for all used modulation formats for SVD and SVD with RT schemes with: (a)–(c) (s_1, s_2) plane; (d)–(f) (s_1, s_3) plane; and (g)–(i) (s_2, s_3) plane.

modulation formats for both images and their RTs. The RT provides more distinguishable SVs for all formats, which is reflected in the results obtained with 1024 samples.

B. Simulation and Experimental Results with 1024 Samples

Figure 11 reveals the accuracy versus the OSNR for the obtained optical signals with 1024 samples in the simulation and experimental scenarios, neglecting the effects of PN and SoP. For the three planes, the DT and KNN classifiers provide higher accuracy levels than those of the SVM classifier. High-order modulation formats require very high OSNRs to be identified, as a large number of ordered points is required. The RTs provide higher accuracy levels than those achieved with the projected images themselves.

For the (s_1, s_2) plane with the DT classifier, 20 dB are required to get a 100% accuracy level for the RTs of the 4-QAM modulation. The 16-QAM modulation needs 20 dB to get a 98% accuracy level. With the KNN classifier, 20 dB are required with 4-QAM and 16-QAM to reach a 98% accuracy level with both schemes. With the SVM classifier, 4-QAM is not well identified with the RT, while the SVDs of the images require 24 dB to reach a 96% accuracy level. The 16-QAM requires 24 dB to reach a 98% accuracy level.

For the (s_1, s_3) plane, the three classifiers provide high accuracy of identification compared to those with the (s_1, s_2) plane. The DT and KNN classifiers achieve higher accuracy levels than those of the SVM classifier. For 4-QAM with the DT classifier, 20 dB are required to reach a 98% accuracy level with the SVD scheme, 28 dB are required with the 16-QAM to reach a 96%
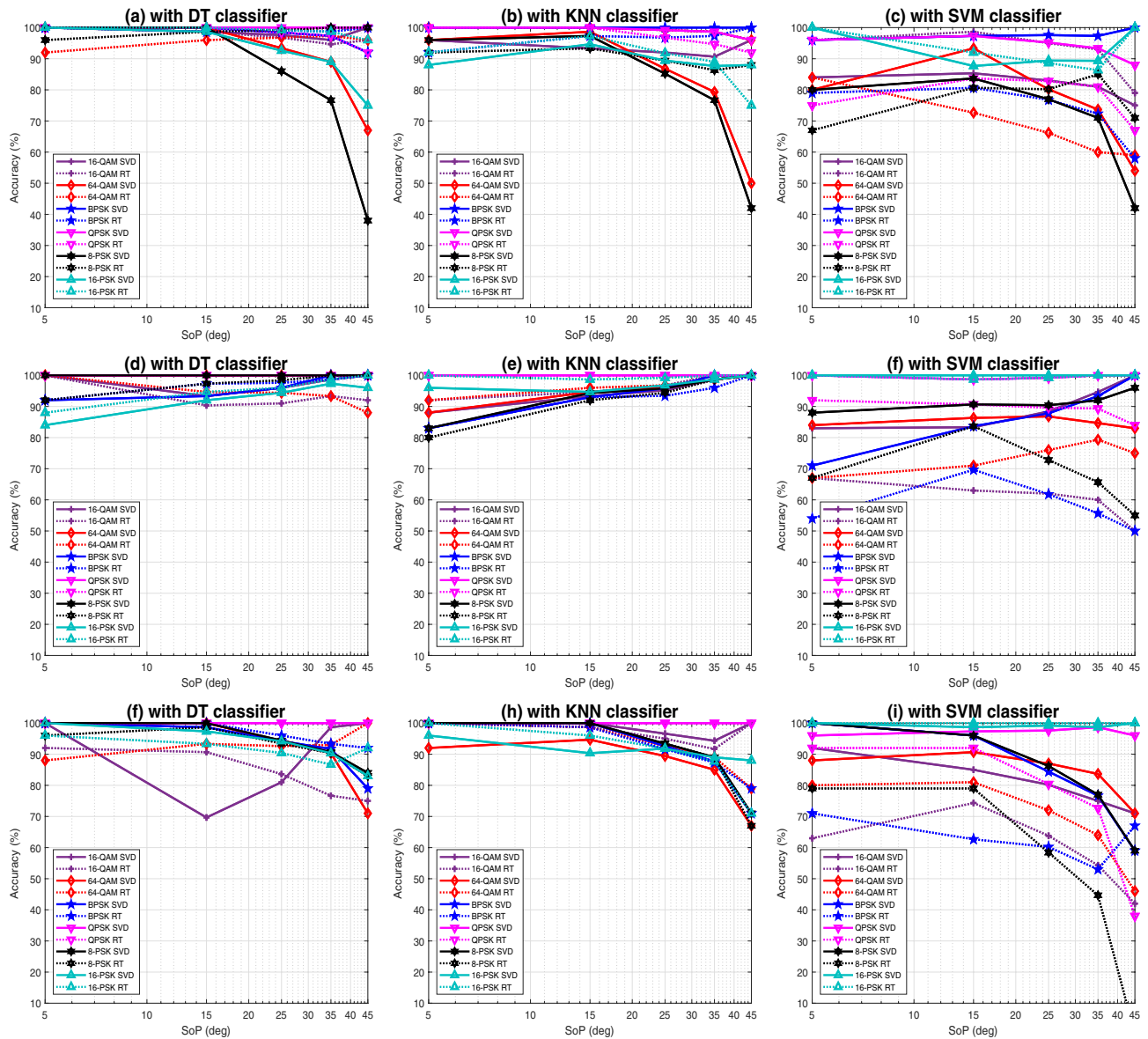
Fig. 16. Accuracy versus SoP levels for all used modulation formats for SVD and SVD with RT schemes with: (a)–(c) (s_1, s_2) plane; (d)–(f) (s_1, s_3) plane; and (g)–(i) (s_2, s_3) plane.

accuracy level. The SVM classifier is not appropriate for the identification in this case.

For the (s_2, s_3) plane, the three classifiers provide high accuracy levels with the two modulation formats. For the DT classifier, 14 dB are required with 4-QAM to reach a 98% accuracy level with the SVD with RT scheme, 12 dB are required to reach a 100% accuracy level with the SVD scheme, and 28 dB are required for 16-QAM to reach a 98% accuracy level. With the KNN classifier, 18 dB are required for 4-QAM to give a 98% accuracy level, and 24 dB are required for 16-QAM to reach a 100% accuracy level. For the SVM classifier, 4-QAM and 16-QAM show stable accuracy levels, and a 16 dB OSNR is required for both to reach a 98% accuracy level.

Figure 12 shows the accuracy versus OSNR from the (s_2, s_3) plane taking the PN effect into consideration. The three classifiers provide high and stable accuracy levels with 4-QAM

and 16-QAM. The results of these classifiers are not good with 64-QAM, as their images are not ordered well in their SS distributions. The distribution image representing each modulation format is distinguishable, especially for the (s_2, s_3) plane images. Also, the RTs of these images are of distinguishable shape, leading to the applicability of MFI at different PN levels.

Figure 13 shows the accuracy versus OSNR from the (s_2, s_3) plane taking the decimation effect of the projected images into consideration. Both decimation by two and decimation by four are studied here. It is clear that the accuracy is still stable and of high level with the three classifiers for 4-QAM and 16-QAM for the three planes of projection. The decimation reduces the sizes of the images leading to less SVs.

Figure 14 shows the accuracy versus OSNR with the (s_2, s_3) plane for the decimated images with different PN levels. The

Table 1. Required OSNR with 1024 Samples for an Accuracy Level Above 98% with the Proposed Schemes in Both Jones Space and SS

		4-QAM				16-QAM			
		SVD		SVD with RT		SVD		SVD with RT	
Used Scheme									
Used Classifier		DT	KNN	DT	KNN	DT	KNN	DT	KNN
Jones space [14]	1 kHz	11 dB	11 dB	11 dB	11 dB	11 dB	11 dB	11 dB	11 dB
	10 kHz	11 dB	11 dB	11 dB	11 dB	11 dB	11 dB	11 dB	11 dB
	100 kHz	11 dB	14 dB	11 dB	11 dB	11 dB	14 dB	11 dB	11 dB
	1 MHz	23 dB	21 dB	11 dB	11 dB	23 dB	22 dB	11 dB	11 dB
(s_1, s_2) plane	1 kHz	26 dB	27 dB	20 dB	19 dB	28 dB	27 dB	27 dB	27 dB
	10 kHz	27 dB	27 dB	21 dB	20 dB	28 dB	27 dB	28 dB	27 dB
	100 kHz	25 dB	28 dB	19 dB	20 dB	>30 dB	30 dB	28 dB	27 dB
	1 MHz	14 dB	24 dB	13 dB	15 dB	23 dB	>30 dB	28 dB	28 dB
(s_1, s_3) plane	1 kHz	25 dB	26 dB	19 dB	20 dB	22 dB	>30 dB	28 dB	25 dB
	10 kHz	25 dB	27 dB	19 dB	19 dB	>30 dB	30 dB	29 dB	28 dB
	100 kHz	26 dB	26 dB	19 dB	19 dB	19 dB	24 dB	22 dB	23 dB
	1 MHz	12 dB	24 dB	15 dB	16 dB	>30 dB	26 dB	24 dB	26 dB
(s_2, s_3) plane	1 kHz	13 dB	21 dB	14 dB	16 dB	27 dB	>30 dB	27 dB	25 dB
	10 kHz	13 dB	17 dB	13 dB	17 dB	>30 dB	28 dB	>30 dB	28 dB
	100 kHz	16 dB	19 dB	14 dB	16 dB	13 dB	>30 dB	13 dB	22 dB
	1 MHz	12 dB	21 dB	13 dB	18 dB	22 dB	27 dB	>30 dB	27 dB

accuracy is better than those with the (s_1, s_2) and (s_1, s_3) planes for all cases with 4-QAM and 16-QAM.

Figure 15 presents the accuracy versus the PN level from the (s_1, s_2), (s_1, s_3), and (s_2, s_3) planes with the three classifiers for six modulation formats. The PN takes the values of 1 kHz, 10 kHz, 100 kHz, 1 MHz, and 10 MHz, and the OSNR is constant at 30 dB for all modulation formats.

Figure 16 presents the SoP effect on the accuracy level for the identification of six modulation formats. The DT and KNN classifiers provide better accuracy levels for all six modulation formats from the three planes with SoP and PN effects, especially from the (s_2, s_3) plane.

The SVM classifier requires the features to be separated from each other with nearly a line separating each class from the other. The SVs for each modulation format are not able to provide a line separating each cluster of points, but with the DT or KNN, the feature points can be separated from each other for each modulation format. The SVs of the SS images or their RTs are distinctive. This leads to high accuracy levels with the DT and KNN classifiers compared to the SVM classifier, due to the fact that the DT and KNN classifiers can provide high accuracy levels for this type of distinctive digital data. The SVM can also provide high accuracy for this type of data but less than those of the DT or KNN classifiers. The average SVs for four modulation formats versus the SV index are presented in Fig. 10, which provides an explanation of why the SVs can be represented by a tree of distributions to be distinguished with the DT or KNN classifiers. The SVD with RT scheme with the DT and KNN classifiers provides better accuracy levels than those with the SVD only. The SVM classifier does not provide the required results with the SVD or the SVD with RT scheme. Also, the SVD with RT is better and more stable with the high PN effect compared to the SVD scheme.

In [14], both schemes are applied on constellation diagrams of different types of modulation formats in Jones space representation. Table 1 summarizes this comparison using the DT and KNN classifiers with 1024 samples for the schemes in Jones space and SS.

A comparison between MFI with SVD and SVD with RT schemes on the constellation diagrams in Jones space in [14] and of the projected images in the SS is presented here. This comparison is performed for two types of modulation only, namely, 4-QAM and 16-QAM, as they are DP modulation formats. It is clear from the numerical results that at different levels of PN and SoP, the projected images in the SS are approximately of high similarity to the original ones. The slight variations provide approximately constant accuracy levels. In Jones space, the accuracy is of high levels even at low levels of OSNR and high levels of PN and SoP. Both 4-QAM and 16-QAM achieve good accuracy levels with the Jones space at lower OSNRs. The (s_2, s_3) plane of the SS provides the same accuracy levels as those of the Jones space for the two modulation formats at higher OSNR values. The 64-QAM achieves good accuracy levels from Jones space, but with the SS the accuracy levels are not good, as a high level of OSNR is required for the same number of samples. Both (s_1, s_2) and (s_1, s_3) planes achieve good accuracy levels for both 4-QAM and 16-QAM. It is clear that the SVD with RT scheme provides good accuracy levels with both SS and Jones space. For the decimation process, the Jones space provides similar accuracy levels to those of the SS for both 4-QAM and 16-QAM.

7. CONCLUSION

Stokes space analysis schemes have been proposed and investigated for MFI. This space originates from the projection of the optical data on three planes. These projections are treated as images, from which signatures of the type of modulation

format are extracted. Two schemes, SVD and SVD with RT, have been investigated for signature extraction of modulation formats. Simulation and experimental results have proved that SS is preferred to Jones space for MFI in the case of high SoP and high levels of PN with low-order modulation formats.

Disclosures. The authors declare no conflicts of interest.

REFERENCES

1. M. C. Tan, F. N. Khan, W. H. Al-Arashi, Y. Zhou, and A. P. T. Lau, "Simultaneous optical performance monitoring and modulation format/bit-rate identification using principal component analysis," J. Opt. Commun. Netw. **6**, 441–448 (2014).
2. D. Zibar, M. Piels, R. Jones, and C. G. Schäeffer, "Machine learning techniques in optical communication," J. Lightwave Technol. **34**, 1442–1452 (2015).
3. O. A. Dobre, A. Abdi, Y. Bar-Ness, and W. Su, "Blind modulation classification: a concept whose time has come," in *IEEE/Sarnoff Symposium on Advances in Wired and Wireless Communication* (IEEE, 2005), pp. 223–228.
4. P. J. Winzer and R.-J. Essiambre, "Advanced optical modulation formats," in *Optical Fiber Telecommunications VB* (Elsevier, 2008), pp. 23–93.
5. F. Musumeci, C. Rottondi, A. Nag, I. Macaluso, D. Zibar, M. Ruffini, and M. Tornatore, "An overview on application of machine learning techniques in optical networks," Commun. Surveys Tuts. **21**, 1383–1408 (2018).
6. I. Martn, S. Troia, J. A. Hernández, A. Rodrguez, F. Musumeci, G. Maier, R. Alvizu, and Ó. G. de Dios, "Machine learning-based routing and wavelength assignment in software-defined optical networks," IEEE Trans. Netw. Serv. Manage. **16**, 871–883 (2019).
7. A. Nag, M. Tornatore, and B. Mukherjee, "Optical network design with mixed line rates and multiple modulation formats," J. Lightwave Technol. **28**, 466–475 (2009).
8. Z. Zhu and A. K. Nandi, *Automatic Modulation Classification: Principles, Algorithms and Applications* (John Wiley & Sons, 2015).
9. M. Xiang, Q. Zhuge, M. Qiu, X. Zhou, M. Tang, D. Liu, S. Fu, and D. V. Plant, "RF-pilot aided modulation format identification for hitless coherent transceiver," Opt. Express **25**, 463–471 (2017).
10. S. Fu, Z. Xu, J. Lu, H. Jiang, Q. Wu, Z. Hu, M. Tang, D. Liu, and C. C.-K. Chan, "Modulation format identification enabled by the digital frequency-offset loading technique for hitless coherent transceiver," Opt. Express **26**, 7288–7296 (2018).
11. E. J. Adles, M. L. Dennis, W. R. Johnson, T. P. McKenna, C. R. Menyuk, J. E. Sluz, R. M. Sova, M. G. Taylor, and R. A. Venkat, "Blind optical modulation format identification from physical layer characteristics," J. Lightwave Technol. **32**, 1501–1509 (2014).
12. S. M. Bilal, G. Bosco, Z. Dong, A. P. T. Lau, and C. Lu, "Blind modulation format identification for digital coherent receivers," Opt. Express **23**, 26769–26778 (2015).
13. G. Liu, R. Proietti, K. Zhang, H. Lu, and S. B. Yoo, "Blind modulation format identification using nonlinear power transformation," Opt. Express **25**, 30895–30904 (2017).
14. R. A. Eltaieb, A. E. Farghal, H. E.-D. H. Ahmed, W. S. Saif, A. M. Ragheb, S. Alshebeili, H. M. Shalaby, and F. A. El-Samie, "Efficient classification of optical modulation formats based on singular value decomposition and radon transformation," J. Lightwave Technol. **38**, 619–631 (2019).
15. M. Hao, L. Yan, A. Yi, L. Jiang, Y. Pan, W. Pan, and B. Luo, "Stokes space modulation format identification for optical signals using probabilistic neural network," IEEE Photon. J. **10**, 1–13 (2018).
16. R. Boada, R. Borkowski, and I. T. Monroy, "Clustering algorithms for Stokes space modulation format recognition," Opt. Express **23**, 15521–15531 (2015).
17. L. Jiang, L. Yan, A. Yi, Y. Pan, T. Bo, M. Hao, W. Pan, and B. Luo, "Blind density-peak-based modulation format identification for elastic optical networks," J. Lightwave Technol. **36**, 2850–2858 (2018).
18. P. Chen, J. Liu, X. Wu, K. Zhong, and X. Mai, "Subtraction-clustering-based modulation format identification in Stokes space," IEEE Photon. Technol. Lett. **29**, 1439–1442 (2017).
19. B. Szafraniec, B. Nebendahl, and T. Marshall, "Polarization demultiplexing in Stokes space," Opt. Express **18**, 17928–17939 (2010).
20. P. Isautier, K. Mehta, A. J. Stark, and S. E. Ralph, "Robust architecture for autonomous coherent optical receivers," J. Opt. Commun. Netw. **7**, 864–874 (2015).
21. F. E. A. El-Samie, "Information security for automatic speaker identification," in *Information Security for Automatic Speaker Identification* (Springer, 2011), pp. 1–122.
22. S. Kolouri, S. R. Park, and G. K. Rohde, "The radon cumulative distribution transform and its application to image classification," IEEE Trans. Image Process. **25**, 920–934 (2015).
23. A. Khatami, M. Babaie, A. Khosravi, H. R. Tizhoosh, S. M. Salaken, and S. Nahavandi, "A deep-structural medical image classification for a radon-based image retrieval," in *30th Canadian Conference on Electrical and Computer Engineering (CCECE)* (IEEE, 2017), pp. 1–4.
24. J. H. Shin, J. H. Jung, and J. K. Paik, "Regularized iterative image interpolation and its application to spatially scalable coding," IEEE Trans. Consum. Electron. **44**, 1042–1047 (1998).
25. O. Fontenla-Romero, B. Pérez-Sánchez, and B. Guijarro-Berdiñas, "LANN-SVD: a non-iterative svd-based learning algorithm for one-layer neural networks," IEEE Trans. Neural Netw. Learn. Syst. **29**, 3900–3905 (2017).